

Optimal Path Planning for Stereotactic Neurosurgery based on an Elastostatic Cannula Model[★]

Philipp Sauerteig^{*} Matthias K. Hoffmann^{**}
 Julian Mühlenhoff^{***} Giovanni Miccoli^{****} Dörthe Keiner^{****}
 Steffi Urbschat^{****} Joachim Oertel^{****} Thomas Sattel^{***}
 Kathrin Flaßkamp^{**} Karl Worthmann^{*}

^{*} *Institute for Mathematics, Technische Universität Ilmenau, Ilmenau, Germany, (e-mail: philipp.sauerteig@tu-ilmenau.de)*

^{**} *Modeling and Simulation, Saarland University, Saarbrücken, Germany*

^{***} *Mechatronics Group, Technische Universität Ilmenau, Ilmenau, Germany*

^{****} *Saarland University Medical Center and Faculty of Medicine, Homburg-Saar, Germany*

Abstract: In this paper, we propose a path-planning problem for stereotactic neurosurgery using concentric tube robots. The main goal is to reach a given region of interest inside the brain, e.g. a tumor, starting from a feasible point on the skull with an ideally short path avoiding certain sensitive brain areas. To describe the shape of the entire cannula from an entry point to the point of interest we use an existing mechanical model for continuum robots. We show numerically that our approach enables the surgeon to reach areas within the brain that would be impossible with a straight cannula as it is currently state of the art.

Copyright © 2022 The Authors. This is an open access article under the CC BY-NC-ND license (<https://creativecommons.org/licenses/by-nc-nd/4.0/>)

Keywords: optimal path planning, concentric tube robots, stereotactic neurosurgery

1. INTRODUCTION

Stereotactic neurosurgical procedures are performed with highly precise surgical instruments designed for deep-seated and small structures. Besides stereotactic biopsy, deep brain stimulation (DBS) is performed in patients with movement disorders such as Parkinson's disease as well as psychiatric disorders. Today, stereotactic procedures are performed with a planning software system based on computer tomography and magnetic resonance imaging (MRI) data to identify targets and obstacles. This allows to precisely compute the point for entering small cannulae or electrodes towards a deep-seated brain structure. So far, stereotactic neurosurgery has been limited to straight cannulae. However, traversing of brain's eloquent areas or vessels needs to be avoided. Thus, in case of brain atrophy and / or a distorted anatomy caused by the underlying disease, it can be difficult to plan a safe and feasible trajectory. As a remedy, recent research works suggest the use of concentric tube robots which are able to form curved trajectories with high precision, enabling minimally invasive surgery in such cases.

Concentric tube robots (CTRs) and their medical applications have developed rapidly over the last decades as elaborated by Gilbert et al. (2016); Bergeles et al. (2015). A general kinematic model for CTRs incorporating tube bending and torsion was derived by Dupont et al. (2010).

[★] This work is funded by the German Research Foundation (DFG, grants FL 989/5-1, OE 253/7-1, SA 773/10-1, WO 2056/11-1).

Torres and Alterovitz (2011) addressed torsional interaction among tubes as well as uncertainty in actuation and in the predicted device shape. They verified their findings in a numerical case study on brain surgery. A software architecture for interactive path planning as well as intra-operatively surgical control for CTRs has been developed by Leibbrandt et al. (2017). Optimal parameter design for CTRs has been studied, e.g. by Burgner et al. (2013).

Regarding validity of planned paths compared to the real robot's behavior, the CTR's mechanical model used for optimization is of a crucial point. Granna et al. (2019) restrict their design space to a two-tube robot with dominating stiffness of the outer tube and are for that reason able to use a purely geometric model. Rucker (2011) as well as Webster et al. (2006) incorporate linear elastostatic effects due to bending and torsion of the tubes, while the latter neglects the torsional component in curved sections of the CTR. Recent modeling approaches aim at reproducing additional nonlinear effects like hysteresis and friction, c.f. Greiner-Petter and Sattel (2017) and Ha et al. (2018). However, for the purpose of path planning, nonlinear models seem to be too computational-heavy without being combined with elastostatic models, so, in a first step, the model of Rucker should be used throughout this paper.

Optimal path planning has been studied numerically as well as in theory for decades, see, e.g. Kambhampati and Davis (1986) and the survey article by Betts (1998). Still, it is a vivid field of research within various applications like

autonomous driving (e.g. Blackmore et al. (2011)) and mobile robots (e.g. Low et al. (2019)). Optimal path planning for mobile robots subject to uncertainty has been studied by van den Berg et al. (2011). Moreover, Faulwassser et al. (2021) derived sufficient stability conditions for predictive path-following control of differentially flat systems.

From MRI data to an optimal path there are many steps to be considered. Figure 1 highlights this paper's contribution to the surgery planning process. Once the region of interest and risk areas are identified and modeled as constraints, an optimal trajectory for the curved cannula can be computed. In this paper, we focus on the path planning

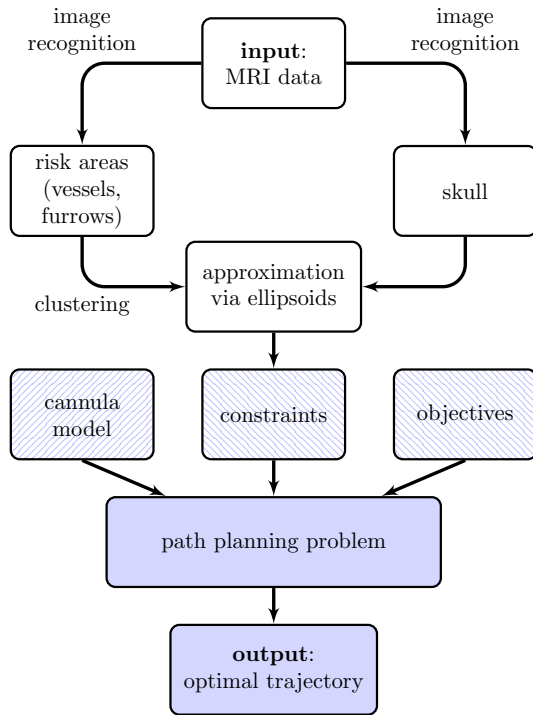


Fig. 1. Embedding of the current paper within the overall approach. Based on post-processed MRI data constraints in form of desired terminal region and obstacles are determined. In combination with an existing cannula model and tailored objectives the path planning problem is formulated. Then, an optimal cannula trajectory is derived numerically.

problem. Based on previous works by Flaßkamp et al. (2019) and Hackenberg et al. (2021), in this contribution, a mechanical system model for the cannula is studied on the basis of the CTR model presented by Rucker et al. (2010). This model accounts for several important aspects from a mechanical point of view like the elastostatic interaction among concentric tubes. While this poses challenges on a suitable planning method in terms of computational complexity, obtained solutions have a higher consensus to a realization of the cannula in future experiments, unlike those corresponding to the highly simplified models used in Flaßkamp et al. (2019) and Hackenberg et al. (2021).

This paper is structured as follows. First, we present the cannula model in Section 2. Then, in Section 3, we formulate the path planning problem, which is solved in

Section 4. Section 5 concludes the paper and outlines next steps.

Notation: We use the isomorphic transformation $\tau : \mathbb{R}^3 \rightarrow \mathbb{R}^{3 \times 3}$

$$\tau(x) = \begin{bmatrix} 0 & -x_3 & x_2 \\ x_3 & 0 & -x_1 \\ -x_2 & x_1 & 0 \end{bmatrix}$$

to map a 3-dimensional vector $x = (x_1, x_2, x_3)^\top$ to a skew-symmetric 3×3 matrix, where $e_3 = (0, 0, 1)^\top$ denotes the third canonical unit vector in \mathbb{R}^3 . Moreover, we use the short-hand notation $[m : n] := \{m, m + 1, \dots, n\}$ for $m, n \in \mathbb{N}$.

2. MODEL DESCRIPTION

We consider the model for concentric tube robots (CTRs) studied by Rucker et al. (2010). A detailed derivation of the model used throughout this paper is given in Section 3 of the thesis by Rucker (2011).

The modeled robot consists of an actuation unit and n , $n \in \mathbb{N}$, concentric tubes. We use index i , $i \in \{1, \dots, n\}$, to denote the tubes in descending order of their diameters, i.e. from the outermost to the innermost. Each tube is fixated within the actuation unit. The base of tube i is located at $\beta_i \leq 0$ while the tip extends to $\ell_i \geq 0$. Furthermore, the tube is rotated around its local z -axis by $\alpha_i \in [0, 2\pi)$, see also Figure 2. The total length of tube i is given by

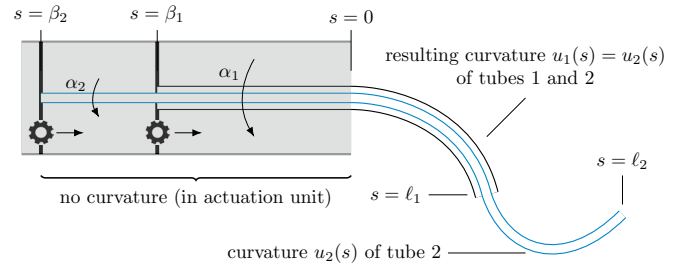


Fig. 2. Example of CTR consisting of $n = 2$ pre-curved, concentric tubes, fixated in the actuation unit and extended to ℓ_1 and ℓ_2 , respectively. The tubes are actuated at their bases with β_1 and β_2 and rotated with α_1 and α_2 , respectively. By design, the paths coincide for $s \leq \ell_1$ and are straight within the actuation unit.

$L_i := \ell_i - \beta_i > 0$ and the length of the entire cannula is $\bar{L} := \max_i \ell_i - \min_j \beta_j$. We assume that the cross section of each rod is circular with constant (inner and outer) diameter for simplification. To avoid tissue damage that would occur because of curvature changes in unactuated tubes, the inner tubes are actuated simultaneously with the outer tubes. Therefore, we set $\bar{\ell} := \max_i \ell_i = \ell_n$, the length of the visible part of the entire cannula, equal to the length of the innermost tube n . In Figure 2, for instance, increasing β_2 , i.e. moving the base of tube 2 to the right, would push the inner tube further through the outer tube and, thus, increase $\ell_2 = \bar{\ell}$. Similar, we use the short-hand notation $\bar{\beta} := \min_i \beta_i$. By $s \in [\bar{\beta}, \bar{\ell}]$ we denote the arc length along the backbone of the cannula. We further use the notation $\dot{\chi}(s)$ to describe the derivative of a quantity χ with respect to the location s along the backbone.

Based on the assumption of constant cross sections per rod, we further set the second moment of area, I_i , of the rod's cross section about the body frame's x or y axis to be constant over the length of the tube. We denote the set of tubes with length at least $s \geq 0$ by $T(s) = \{i \in [1:n] \mid \ell_i \geq s\}$. A single tube i is fully described by its total length L_i , its pre-curvature $u_i^* \in \mathbb{R}^3$ and the actuation (α_i, β_i) . The pre-curvature denotes how strongly the tube bends around the axes of a given coordinate system, when no load is put on the tube. However, when being combined into one cannula, each tube affects the elastostatic curvature of all other tubes. To describe this interaction, let $\psi_i(s)$ denote the rotation of rod i around its local z -axis at arc length s and split the curvature vector $u_i = (u_{ix}, u_{iy}, u_{iz})^\top$ into $u_{ixy} = (u_{ix}, u_{iy})^\top$ and u_{iz} . In other words, u_{ixy} describes the amount how much the tube bends away from a straight tube, while u_{iz} specifies how twisted the tube is. Then, the interaction of the tubes among each other can be described by

$$\dot{\psi}_i(s) = u_{iz}(s) \quad (1a)$$

$$\dot{u}_{iz}(s) = \frac{E_i I_i}{(EI)(s) G_i J_i} \sum_{j \in T(s)} E_j I_j (u_{ixy}^*)^\top B_{\psi_{ij}}(s) u_{jxy}^* \quad (1b)$$

for $s \leq \ell_i$ with $(EI)(s) := \sum_{i \in T(s)} E_i I_i$ and

$$B_{\psi_{ij}}(s) = \begin{bmatrix} \sin(\psi_i(s) - \psi_j(s)) & -\cos(\psi_i(s) - \psi_j(s)) \\ \cos(\psi_i(s) - \psi_j(s)) & \sin(\psi_i(s) - \psi_j(s)) \end{bmatrix}.$$

Here, the parameters E_i , G_i , and J_i describe Young's modulus, the shear modulus and the polar moment $J_i = 2I_i$. Note that, in Figure 2 for instance, tube 1 does not (immediately) affect tube 2 at $s > \ell_1$ since $T(s) = \{2\}$ on this section of the cannula. The initial condition of each tube at the actuation unit is given by its curvature and the corresponding actuation variables as

$$\psi_i(0) = \alpha_i - \beta_i u_{iz}(0), \quad (1c)$$

which describes the torsion on the section $[\beta_i, 0]$ inside the actuation unit. At the end of each tube we assume the torsion-free boundary condition

$$u_{iz}(\ell_i) = 0 \quad (1d)$$

since we do not consider external loads. Thus, equations (1) form a boundary value problem (BVP). Furthermore, the remaining x and y component of the curvature u_i of tube i is given by the algebraic equation

$$u_{ixy}(s) = \frac{1}{(EI)(s)} \sum_{j \in T(s)} R_{\psi_j - \psi_i}(s) E_j I_j u_{jxy}^* \quad (2)$$

with matrix $R_{\psi_j - \psi_i}(s)$ defined as

$$R_{\psi_j - \psi_i}(s) = \begin{bmatrix} \cos(\psi_j(s) - \psi_i(s)) & -\sin(\psi_j(s) - \psi_i(s)) \\ \sin(\psi_j(s) - \psi_i(s)) & \cos(\psi_j(s) - \psi_i(s)) \end{bmatrix}$$

for all s .

Let

$$\text{SO}(3) := \{R \in \mathbb{R}^{3 \times 3} \mid R^\top R = I, \det(R) = 1\}$$

denote the special orthogonal group in 3 dimensions. Based on $u_i(s)$, the position $p_i(s) \in \mathbb{R}^3$ and orientation $R_i(s) \in \text{SO}(3)$ of a piece of tube parameterized by s can be computed via the initial value problem

$$\dot{p}_i(s) = R_i(s) \cdot e_3, \quad p_i(0) = p_i^0 \quad (3a)$$

$$\dot{R}_i(s) = R_i(s) \cdot \tau(u_i(s)), \quad R_i(0) = R_i^0, \quad (3b)$$

where $e_3 = (0, 0, 1)^\top$ denotes the third canonical unit vector in \mathbb{R}^3 .

3. PROBLEM FORMULATION

In this paper, we focus on the path planning process, i.e., we determine an optimal path from the entry region ($s = 0$) to the desired terminal point $p_f \in \mathbb{R}^3$ or terminal region $\mathbb{P}_f \subset \mathbb{R}^3$ ($s = \ell_n$) as depicted in Figure 3, while respecting the physical model. The dynamical process of

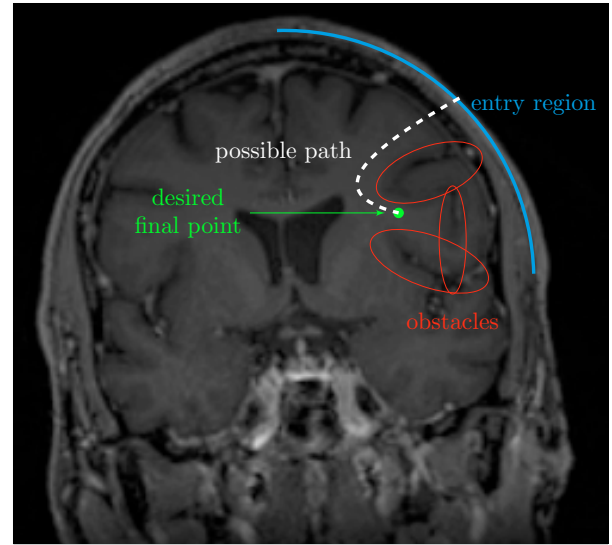


Fig. 3. Example MRI footage of a skull. The red ellipses depict outer approximations of sensitive brain areas (here: furrows) and need to be avoided by the cannula. The desired final point (green dot) is located behind the obstacles, such that a stereotactic procedure with straight cannula (within this 2D plane) would cause severe damage. As a remedy, the white dashed line depicts a possible curved trajectory to reach the tumor without crossing the sensitive regions.

extending the tubes until this position is reached and the associated difficulties like violation of the follow-the-leader behaviour, as it is e.g. done by Flaßkamp et al. (2019), and hysteresis effects will be included in future work.

The main objective is to reach the terminal set \mathbb{P}_f with the cannula tip without causing damage to sensitive areas, in particular vessels and furrows. We assume outer approximations of those areas to be given in form of ellipsoids \mathcal{E}_k , $k \in [1:K]$, with $K \in \mathbb{N}$ being the number of high-risk areas. We further write $\mathcal{E} = \mathcal{E}_1 \cup \dots \cup \mathcal{E}_K$ and denote the skull (with its interior) by $\mathcal{S} \subset \mathbb{R}^3$. For computing these ellipsoids, we refer to Hackenberg et al. (2021). Additionally, we either aim to minimize the total length of the path in order to reduce the risk of severe brain damage by minimizing

$$J_1(d) := \ell_n^2 = (L_n + \beta_n)^2$$

or the deviation from the desired final point by minimizing

$$J_2(d) := \|p_n(\ell_n) - p_f\|_2^2.$$

Here, $d = (p_n^0, R_n^0, L, u^*, \alpha, \beta)$ collects all optimization variables with $u^* = (u_1^*, \dots, u_n^*)$ and analogous for the other variables. We choose quadratic penalization since, as

it is well known in other applications, we observed more robust numerical behavior compared to other norms.

The cannula's mechanics are taken into account as constraints in the optimization problem. Since the tubes are concentric by assumption, it suffices to consider position and orientation of the longest tube. As we further assume to always extend the inner tubes along with the outer tubes, we take only p_n and R_n into account. From here on, we drop the index n and write p and R , respectively.

These considerations motivate the optimal path-planning problem (OP³)

$$\min_{d \in \mathbb{D}_n} J_k(d), \quad (4a)$$

$k \in \{1, 2\}$, subject to the constrained BVP

$$\ell_i = L_i + \beta_i \quad \forall i \in [1:n] \quad (4b)$$

$$p(\ell_n) \in \mathbb{P}_f \quad (4c)$$

$$p(s) \in \mathcal{S} \setminus \mathcal{E} \quad \forall s \in [0, \ell_n] \quad (4d)$$

$$\dot{p}(s) = R(s)e_3 \quad (4e)$$

$$\dot{R}(s) = R(s) \cdot \tau \left(\left(\frac{1}{(EI)(s)} \sum_{j \in T(s)} R_{\psi_j - \psi_n}(s) E_j I_j u_{jxy}^* \right) u_{nz}(s) \right) \quad (4f)$$

$$\dot{\psi}_i(s) = u_{iz}(s) \quad \forall i \in [1:n] \quad (4g)$$

$$\dot{u}_{iz}(s) = \frac{E_i I_i}{(EI)(s) G_i J_i} \sum_{j \in T(s)} E_j I_j (u_{ixy}^*)^\top B_{\psi_{ij}}(s) u_{jxy}^*, \quad \forall i \in [1:n] \quad (4h)$$

$$p(0) = p^0, \quad R(0) = R^0, \quad (4i)$$

$$\psi_i(0) = \alpha_i - \beta_i u_{iz}(0), \quad u_{iz}(\ell_i) = 0 \quad \forall i \in [1:n] \quad (4j)$$

with feasible set

$$\mathbb{D}_n := \left\{ (p^0, R^0, L, u^*, \alpha, \beta) \left| \begin{array}{l} p^0 \in \partial \mathcal{S}, R^0 \in \text{SO}(3) \\ 0 < L_1 \leq \dots \leq L_n \leq \bar{L} \\ 0 \leq \alpha_i < 2\pi \quad \forall i \in [1:n] \\ -L_i \leq \beta_i \leq 0 \quad \forall i \in [1:n] \\ u_i^* \in \mathbb{R}^3 \quad \forall i \in [1:n] \end{array} \right. \right\}.$$

Here, we plugged (2) for $i = n$ into the right-hand side of (4f). We neglect the non-extended part of the tubes, i.e., where $s < 0$, but enforce an initial condition on $p(0)$, $R(0)$ and $\psi_i(0)$ at the entry point. Note that problem (4) is non-convex, thus, the solutions derived in the subsequent sections may be local minima.

4. NUMERICAL CASE STUDY

In this section, we solve the OP³ numerically. Two aspects are focused on: One is the impact of the degree of freedom in the optimization and the other the choice of the objective function on the optimal path.

4.1 Setting and implementation details

A 2D-projection of the considered setting is depicted in Figure 3. We designed ellipsoids \mathcal{E}_i , $i \in \{1, 2, 3\}$, in 3D to approximately fit the red obstacles and placed a ball of radius 0.005 m around the desired final point. The points $q = (q_x, q_y, q_z)^\top$ on the surface of an ellipsoid with center $c_m = (c_{mx}, c_{my}, c_{mz})^\top \in \mathbb{R}^3$ and radii $r_m = (r_{mx}, r_{my}, r_{mz})^\top \in \mathbb{R}_{>0}^3$ are given by the equation

$$\frac{(q_x - c_{mx})^2}{r_{mx}^2} + \frac{(q_y - c_{my})^2}{r_{my}^2} + \frac{(q_z - c_{mz})^2}{r_{mz}^2} = 1.$$

Based on this observation we write constraint (4d) as

$$\frac{(p_x(s) - c_{mx})^2}{r_{mx}^2} + \frac{(p_y(s) - c_{my})^2}{r_{my}^2} + \frac{(p_z(s) - c_{mz})^2}{r_{mz}^2} > 1$$

for all $s \in [0, \ell_n]$ and the upright ellipsoid \mathcal{E}_1 . Additionally, the other two ellipsoids are rotated around the y axis with rotation matrix

$$Q(\gamma_k) = \begin{bmatrix} \cos(\gamma_k) & 0 & \sin(\gamma_k) \\ 0 & 1 & 0 \\ -\sin(\gamma_k) & 0 & \cos(\gamma_k) \end{bmatrix},$$

$k = 2, 3$. We formulate the corresponding constraints as

$$\frac{\hat{p}_x(s)^2}{r_{mx}^2} + \frac{\hat{p}_y(s)^2}{r_{my}^2} + \frac{\hat{p}_z(s)^2}{r_{mz}^2} > 1,$$

where

$$\hat{p}(s) := Q(\gamma_k)^{-1}(p(s) - c_k).$$

The parameters of the three ellipsoidal obstacles implemented in our simulations are listed in Table 1. As a

Table 1. Parameters describing the ellipsoids

k	1	2	3
c_k	$\begin{pmatrix} 0.03392 \\ 0 \\ 0.04067 \end{pmatrix}$	$\begin{pmatrix} 0.0421 \\ 0 \\ 0.0112 \end{pmatrix}$	$\begin{pmatrix} 0.04467 \\ 0 \\ 0.02591 \end{pmatrix}$
r_k	$\begin{pmatrix} 0.00632 \\ 0.04472 \\ 0.01291 \end{pmatrix}$	$\begin{pmatrix} 0.00447 \\ 0.04472 \\ 0.01581 \end{pmatrix}$	$\begin{pmatrix} 0.00447 \\ 0.04472 \\ 0.01826 \end{pmatrix}$
γ_k	45	30	0

simplification, we model the interesting part of the head, i.e. the upper right part in Figure 3, as a quarter of a ball with radius 0.067 m. In our simulations, we restrict ourselves to a fixed number of tubes, namely the case $n = 3$. Furthermore, we choose the total lengths L_i of the tubes to be fix but sufficiently long, since in practice the manufacturable lengths exceed the size of a skull. In the scenarios with optimized pre-curvatures, we restricted them to

$$(0, 0, 0)^\top \leq u_i^* \leq 20 \cdot (1, 1, 1)^\top \text{ m}^{-1} \quad \forall i \in \{1, 2, 3\}.$$

For numerical optimization, we used the `python` toolbox `CasADi` developed by Andersson et al. (2019) with the inherent solver `IPOPT` by Wächter and Biegler (2006). Ordinary differential equations are discretized via the classical fourth-order Runge-Kutta scheme. Note that standard Runge-Kutta does not necessarily maintain structural properties such as the $\text{SO}(3)$ property of R . In our numerical simulations we observed that $1 < \det R(s) < 1.1$ for $s \neq 0$ after some discretization steps, which means that the computed $R(s)$ at the discretization steps are no longer in $\text{SO}(3)$. However, the impact of $\det R(s) = 1.03$ after 150 discretization steps is negligible for a proof of concept such that improved numerical integration is left for future work.

4.2 Numerical results

The results are depicted in Figures 4 to 7. Similar to Figure 3, the red ellipsoids represent (outer approximations of) obstacles \mathcal{E}_k , $k \in \{1, 2, 3\}$. The green ball (radius 0.005m) is the target area P_f that the cannula tip needs to reach. The blue outer grid depicts the skull (ball with radius 0.0673m). The blue, orange, and green curve show the position of the outermost, middle, and innermost tube,

respectively. The curvature optimization with a maximum curvature of 20 m^{-1} is compared to optimization with fixed tube curvatures $u_x = [0.0, 0.0, 0.0]$, $u_y = [0.0, 9.8, 13.8]$ and $u_z = [0, 0, 0] \text{ m}^{-1}$. Moreover, we investigate the impact of the restriction $y \approx 0$ in order to force the trajectory to lie within the $x - z$ plane.

In all cases, the cannula approaches the restricted areas very tightly. In the 3-dimensional case depicted in Figure 4 the cannula slips between two of the restricted areas. This

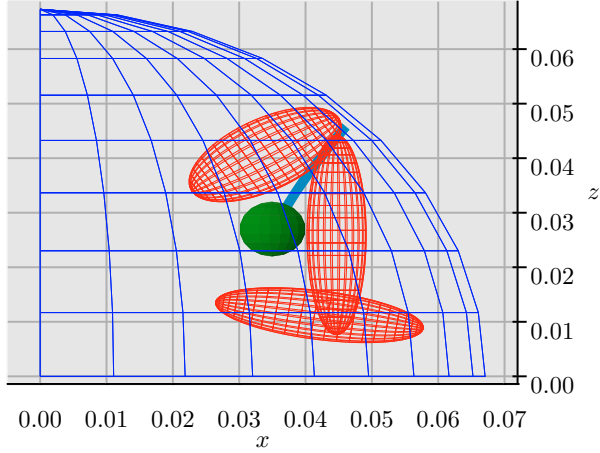


Fig. 4. 3D-solution, where the cannula slips between the ellipsoids.

shows the importance of 3D planning, since a planar design space would not have revealed this solution. However, in order to show the full potential of combining several tubes with varying curvatures, we restrict the entry point to $y \in [0, 0.02]$ in the remainder excluding solutions as depicted in Figure 4.

Figure 5 shows the optimal paths within the $x - z$ plane, once for the optimized and once for the fixed pre-curvatures, when minimizing the total cannula length ℓ_n . The additional degree of freedom allows to reduce the

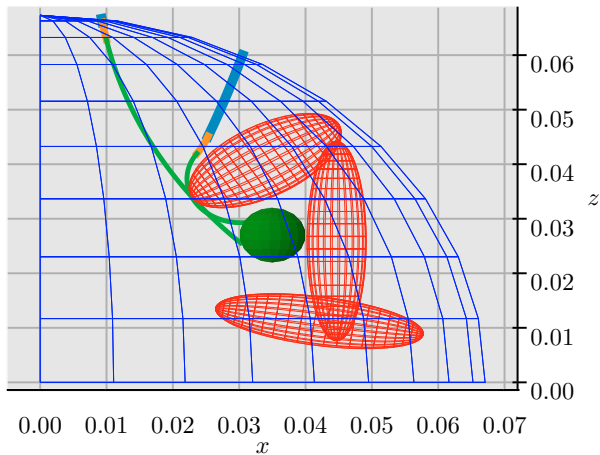


Fig. 5. Solution in the $y = 0$ plane for optimal ($\ell_n = 0.037\text{m}$) and fixed ($\ell_n = 0.047\text{m}$) pre-curvatures, respectively.

cannula length significantly. The solutions in Figure 6 are not restricted to the $x - z$ plane. The trajectories, in

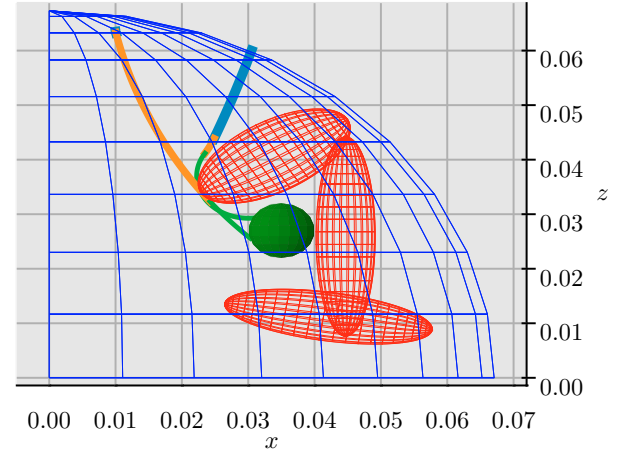


Fig. 6. Solution in 3 dimensions for optimal ($\ell_n = 0.037\text{m}$) and fixed ($\ell_n = 0.047\text{m}$) pre-curvatures, respectively.

particular with optimized pre-curvatures, are very similar to the ones in Figure 5. However, in the case with fixed pre-curvatures, the visible part of the middle tube is bigger than the one of the innermost.

Additionally, Figure 7 illustrates solutions for minimizing the deviation of the cannula tip from the target point neglecting the total cannula length. With free pre-curvatures

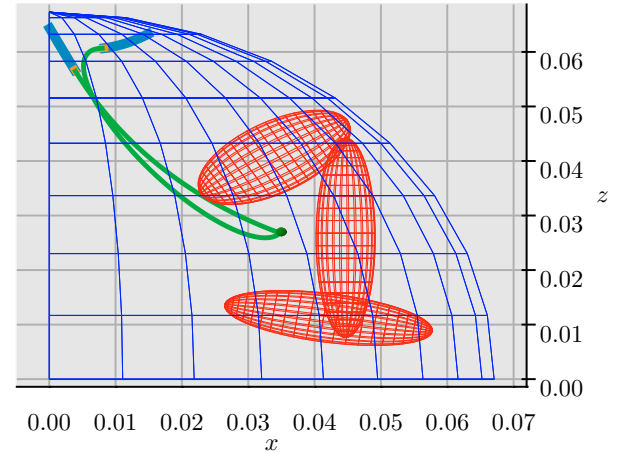


Fig. 7. Solution in the $y = 0$ plane for optimal ($\ell_n = 0.0893\text{m}$ and $p_n(\ell_n) - p_f = 1.36 \cdot 10^{-5}\text{m}$) and fixed ($\ell_n = 0.056\text{m}$ and $p_n(\ell_n) - p_f = 2.8 \cdot 10^{-4}\text{m}$) pre-curvatures, respectively.

it is better to make a slight detour in the beginning to get closer to the target point at the end.

From these results, we conclude that the modeling of risk structures is safety-critical, since the optimal solution tends to touch their borders. Moreover, the length of the cannula and the reachability of goal points seem to conflict each other. Without having J_2 as an objective to minimize, the optimal solution only reaches the boundary of the ball enclosing the entry point due to the corresponding boundary condition. Minimizing J_2 , on the contrary, provides a solution which reaches inside the goal. Moreover, and less intuitive, this solution also qualitatively differs since

it chooses a different path requiring a totally different set-up of tubes.

5. CONCLUSIONS AND OUTLOOK

In this paper, we derived a path-planning problem for stereotactic neurosurgery and solved it numerically. We considered an elastostatic model for concentric tube robots to account for the trajectory of the cannula and combined it with application-motivated constraints and objectives. Our numerical case study shows that the presented approach has the potential to reduce damage during brain surgery by enabling minimally invasive surgery where it previously was not possible.

In the future, we will address several extensions of the presented approach to improve its robustness. In particular, we aim to use structure-preserving integrators to ensure that the orientation matrix $R(s)$ is in $SO(3)$ for all $s \in [0, \ell_n]$ and to compare different discretization approaches with respect to their performance. Furthermore, we aim to apply multiobjective optimization techniques to characterize Pareto optimal points with respect to the objectives minimal cannula length versus minimal tracking error as a decision-making support tool for the surgeon. Also, we will increase β stepwise to model the dynamic extension of the tubes in order to account for effects such as hysteresis and violation of the follow-the-leader behaviour.

REFERENCES

- Andersson, J.A., Gillis, J., Horn, G., Rawlings, J.B., and Diehl, M. (2019). Casadi: a software framework for nonlinear optimization and optimal control. *Mathematical Programming Computation*, 11(1), 1–36. doi:10.1007/s12532-018-0139-4.
- Bergeles, C., Gosline, A.H., Vasilyev, N.V., Codd, P.J., Pedro, J., and Dupont, P.E. (2015). Concentric tube robot design and optimization based on task and anatomical constraints. *IEEE Transactions on Robotics*, 31(1), 67–84. doi:10.1109/TRO.2014.2378431.
- Betts, J. (1998). Survey of numerical methods for trajectory optimization. *J. Guid. Control Dynam*, 21(2), 193–207. doi:10.2514/2.4231.
- Blackmore, L., Ono, M., and Williams, B.C. (2011). Chance-Constrained Optimal Path Planning With Obstacles. *IEEE Transactions on Robotics*, 27(6), 1080–1094. doi:10.1109/TRO.2011.2161160.
- Burgner, J., Gilbert, H.B., and Webster, R.J. (2013). On the computational design of concentric tube robots: Incorporating volume-based objectives. In *2013 IEEE International Conference on Robotics and Automation*, 1193–1198. doi:10.1109/ICRA.2013.6630723.
- Dupont, P.E., Lock, J., Itkowitz, B., and Butler, E. (2010). Design and Control of Concentric-Tube Robots. *IEEE Transactions on Robotics*, 26(2), 209–225. doi:10.1109/TRO.2009.2035740.
- Faulwasser, T., Mehrez, M., and Worthmann, K. (2021). *Predictive Path Following Control Without Terminal Constraints*, 1–26. Springer International Publishing. doi:10.1007/978-3-030-63281-6_1.
- Flaßkamp, K., Worthmann, K., Mühlenhoff, J., Greiner-Petter, C., Büskens, C., Oertel, J., Keiner, D., and Sattel, T. (2019). Towards optimal control of concentric tube robots in stereotactic neurosurgery. *Math. Comput. Model. Dyn. Syst.*, 25(6), 560–574. doi:10.1080/13873954.2019.1690004.
- Gilbert, H.B., Rucker, D.C., and III, R.J.W. (2016). *Concentric Tube Robots: The State of the Art and Future Directions*, volume 114. Springer, Cham. doi:10.1007/978-3-319-28872-7_15.
- Granna, J., Nabavi, A., and Burgner-Kahrs, J. (2019). Computer-assisted planning for a concentric tube robotic system in neurosurgery. 14(2), 335–344. doi:10.1007/s11548-018-1890-8.
- Greiner-Petter, C. and Sattel, T. (2017). On the influence of pseudoelastic material behaviour in planar shape-memory tubular continuum structures. 26(12), 125024. doi:10.1088/1361-665X/aa8dc7.
- Ha, J., Fagogenis, G., and Dupont, P.E. (2018). Modeling tube clearance and bounding the effect of friction in concentric tube robot kinematics. 35(2), 353–370. doi:10.1109/tro.2018.2878906.
- Hackenberg, A., Worthmann, K., Pätz, T., Keiner, D., Oertel, J., and Flaßkamp, K. (2021). Neurosurgery planning based on automated image recognition and optimal path design. *at - Automatisierungstechnik*, 69(8), 708–721. doi:10.1515/auto-2021-0044.
- Kambhampati, S. and Davis, L. (1986). Multiresolution path planning for mobile robots. *IEEE Journal on Robotics and Automation*, 2(3), 135–145. doi:10.1109/JRA.1986.1087051.
- Leibrandt, K., Bergeles, C., and Yang, G.Z. (2017). Concentric Tube Robots: Rapid, Stable Path-Planning and Guidance for Surgical Use. *IEEE Robotics Automation Magazine*, 24(2), 42–53. doi:10.1109/MRA.2017.2680546.
- Low, E.S., Ong, P., and Cheah, K.C. (2019). Solving the optimal path planning of a mobile robot using improved Q-learning. *Rob. Auton. Syst.*, 115, 143–161. doi:10.1016/j.robot.2019.02.013.
- Rucker, D.C. (2011). The Mechanics of Continuum Robots: Model-Based Sensing and Control.
- Rucker, D.C., Jones, B.A., and III, R.J.W. (2010). A Geometrically Exact Model for Externally Loaded Concentric-Tube Continuum Robots. *IEEE Transactions on Robotics*, 26(5), 769–780. doi:10.1109/TRO.2010.2062570.
- Torres, L.G. and Alterovitz, R. (2011). Motion planning for concentric tube robots using mechanics-based models. In *2011 IEEE/RSJ International Conference on Intelligent Robots and Systems*, 5153–5159. doi:10.1109/IROS.2011.6095168.
- van den Berg, J., Abbeel, P., and Goldberg, K. (2011). LQG-MP: Optimized path planning for robots with motion uncertainty and imperfect state information. *Int. J. Robot. Resarch*, 30(7), 895–913. doi:10.1177/0278364911406562.
- Wächter, A. and Biegler, L.T. (2006). On the implementation of an interior point filter line-search algorithm for large-scale nonlinear programming. *Math. Program.*, 106(1), 25–57. doi:10.1007/s10107-004-0559-y.
- Webster, R.J., Okamura, A.M., and Cowan, N.J. (2006). Toward active cannulas: Miniature snake-like surgical robots. In *2006 IEEE/RSJ international conference on intelligent robots and systems*, 2857–2863. IEEE. doi:10.1109/IROS.2006.282073.